



Dual-mode independent detection of pressure and refractive index by miniature grating-coupled surface plasmon sensor

HAIBIN NI,¹ LU ZHANG,¹ AN PING,¹ ALEXEY V. KRASAVIN,²
HASSAN ALI,¹  BO NI,¹ AND JIANHUA CHANG^{1,*}

¹*Jiangsu Key Laboratory of Meteorological Observation and Information Processing, School of Electronic and Information Engineering, Nanjing University of Information Science & Technology, Nanjing 210044, China*

²*Department of Physics and London Centre for Nanotechnology, King's College London, Strand, London WC2R 2LS, UK*

**jianhuachang@nuist.edu.cn*

Abstract: Multiple parameters need to be monitored to analyze the kinetics of biological progresses. Surface plasmon polariton resonance sensors offer a non-invasive approach to continuously detect the local change of refractive index of molecules with high sensitivity. However, the fabrication of miniaturized, compact, and low-cost sensors is still challenging. In this paper, we propose and demonstrate a grating-coupled SPR sensor platform featuring dual mode operation for simultaneous sensing of pressure and refractive index, which can be fabricated using a highly-efficient low-cost method, allowing large-scale production. Both sensing functionalities are realized by optical means via monitoring the spectral positions of a surface plasmon polariton mode (for refractive index sensing) and Fabry-Perot or metal-insulator-metal modes (for pressure sensing), which are supported by the structure. Simultaneous measurement of refractive index with the sensitivity of 494 nm/RIU and pressure was demonstrated experimentally. The proposed platform is promising for biomonitoring that requires both high refractive index sensitivity and local pressure detection.

Published by Optica Publishing Group under the terms of the [Creative Commons Attribution 4.0 License](https://creativecommons.org/licenses/by/4.0/). Further distribution of this work must maintain attribution to the author(s) and the published article's title, journal citation, and DOI.

1. Introduction

Surface plasmon polariton (SPP) is a surface electromagnetic wave produced by coupling of an electromagnetic field to the oscillation of free electron gas at the interface of metallic and dielectric materials [1]. The wavelength of the SPP resonance (SPR) is closely related to the morphology of the metal surface and the local refractive index. A minor change in the local environment (e.g. via binding of biomolecules) results in the modification of the refractive index near the metal film and therefore produces a wavelength shift of the SPR, which makes this resonance a good candidate for optically-monitored sensing. SPR-based sensors have been widely used in drug [2,3], medical diagnostics [4,5], biological molecule detection [6], life sciences [7], and other fields [8,9], due to their prominent advantages, such as label-free operation, high sensitivity and real-time detection [10].

Since there is a wavevector mismatch between a photon and a surface plasmon, a prism-assisted total internal reflection scheme matching the wavevectors or a grating supplying an additional momentum are employed for the excitation of surface plasmons. Kretschmann configuration [11] using a prism coated with a thin metal film is commonly used in commercially available SPR bio-sensors [12–15]. It exhibits high sensitivity but required rather large size of the device, prohibiting its integration. Alternatively, SPR can be excited on periodic metallic nanostructures

in a form of Bloch waves. However, such nanostructures, e.g. metallic gratings may cause non-specific binding of analyte in its periodic grooves [16]. They also cannot provide a physically flat surface for binding of cells and bio-molecular recognition elements (BRE), such as antibodies, peptides and nucleic acids [17,18]. Consequently, conventional surface plasmon polariton sensors are either very large in size in the prim realization or do not possess a desired smooth interface in the periodic one. Joseph et al. [19] proposed an interesting approach of fabrication of a grating coupled plasmon polariton sensor using interference lithography, but further work towards more simple and affordable fabrication methods, e.g. relying on commercially-available low-cost imprinting techniques (instead of interferometry), utilized below together with the increase in the sensor functionality, would be highly beneficial.

In this paper, a grating-coupled surface plasmon sensing platform with a flat sensing surface was proposed and experimentally demonstrated. It utilizes a commercially available low-cost pressure casting method, combined with polymer filling and metal film coating to form a miniature SPR sensor with a smooth sensing surface. While retaining high sensitivity and the flat sensing interface so far realized only in traditional prism-based SPR instruments, the proposed SPR sensor can have a size of just few micrometers and does not require complex optical collimation. Furthermore, another mechanism, utilizing Fabry-Perot (F-P) or metal/insulter/metal modes supported by this configuration was proposed and realized for simultaneous and independent sensing of local pressure. Due to the independent dual sensing modality and the possibility of large scale low-cost fabrication, this sensor offers promising applications in biology, medicine and food safety industry.

2. Device structure design and simulation

A typical grating-coupled SPR sensor configuration is shown in Fig. 1(a). A metallic grating with period P fabricated on a Polycarbonate substrate, is separated from a silver film with thickness d with a spacer layer of Polystyrene (PS) or Polydimethylsiloxane (PDMS) with thickness H (the sum of the upper layer height t and the grating depth h_2). Two types of optical modes excited in this structure upon a TM polarized light illumination, namely an SPP mode and F-P modes will be utilized for sensing. The SPP mode is excited on the top flat surface when the incident TM polarized light is diffracted on the embedded metal grating. The F-P mode formed between the metal film and the metallic grating is dependent on the thickness t of spacer layer (which will be used in pressure sensing making it from an elastic material), and is insensitive to the changes in the outer environment. In contrast, the SPP resonance is strongly dependent on the periodicity P of the embedded metal grating and the refractive index of surrounding material as described by the following equation [20]

$$n_a \sin \theta_a + m \frac{\lambda}{P} = \pm \sqrt{\frac{\epsilon_m \epsilon_d}{\epsilon_m + \epsilon_d}}, \quad (1)$$

where n_a is the refractive index of the incident medium, θ_a is the incident angle, m is the diffraction order, P is the grating period, ϵ_m and ϵ_d are the dielectric constants of the metal layer and dielectric layer, respectively.

Finite-difference time-domain (FDTD) algorithm was employed to simulate the optical properties of the structure [21]. The structural parameters were selected to be $P = 740$ nm, $h_1 = 125$ nm, $h_2 = 85$ nm, $t = 280$ nm and $d = 25$ nm. Refractive indices of Polycarbonate substrate, Polystyrene and Polydimethylsiloxane were approximated taken as 1.584, 1.56 and 1.4 [22], respectively, while the dielectric constant of silver is taken from Palik [23]. Periodic boundary conditions were applied in the x and y directions, while PML boundary conditions was set in the z direction. Mesh size in all directions was chosen to be 3 nm. For PS spacer, the calculated reflectance spectra of the structure at normal incidence is shown in Fig. 1(b).

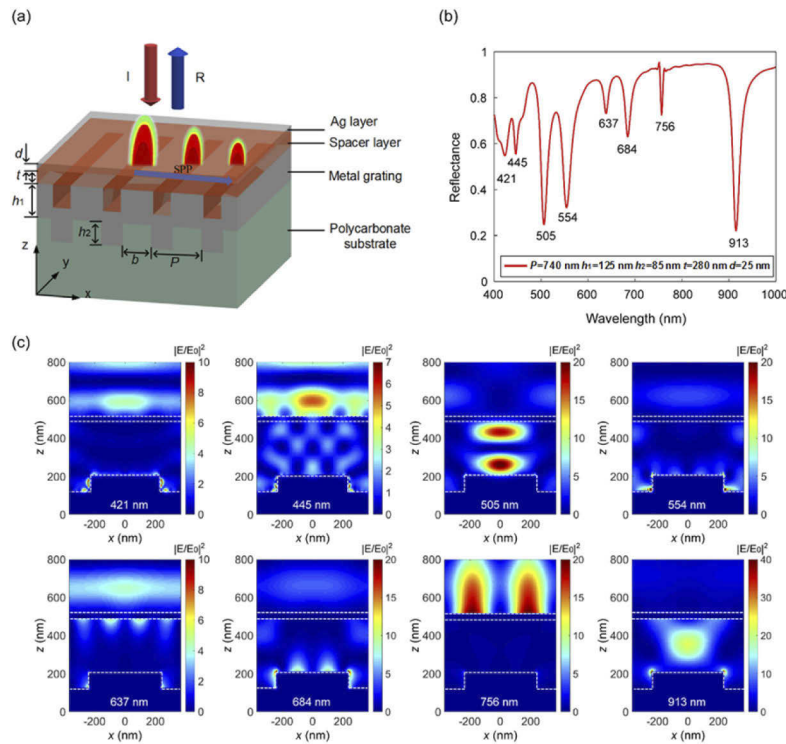


Fig. 1. Dual-mode grating-coupled SPR sensor: (a) Schematic diagram of the sensor. (b) Reflection spectrum simulated under normal incidence revealing optical modes supported by the structure with $P = 740$ nm, $h_1 = 125$ nm, $h_2 = 85$ nm, $t = 280$ nm and $d = 25$ nm. (c) Electrical field distributions of the resonant modes.

There are eight reflectance dips in the spectra, the simulated electric field distributions at the corresponding wavelengths present the excitation of various resonant modes (Fig. 1(c)). Featuring enhanced electric fields at the top surface of the silver film, the electrical field distributions at 756 nm and 445 nm wavelengths indicate the excitation of SPP modes on the top metal-air interface, generated via the first and the second order diffraction of the incident wave on the grating, respectively. Analogously, the reflection dip at 637 nm corresponds to the excitation of an SPP mode at the bottom metal-polymer interface of the film, generated via the second order diffraction (the mode corresponding to the first order of the diffraction lies beyond the studied wavelength range and located further in the IR). On the other hand, the electric field distributions indicate that the modes at 913 nm and 505 nm wavelengths are clearly first- and second-order F-P modes of the cavity produced by the grating and the film. The other three modes correspond to Bloch SPP resonances supported by the metallic grating.

The SPP mode excited at 756 nm, which has a strong field localization at the film surface interfacing the environment and a very narrow resonance is particularly promising for the refractive index sensing. Its nature is further confirmed by current density j_x distribution presented in Fig. 2(a). Confined to the metal/air interface with an electric field exponentially decaying into surroundings, this SPP mode is sensitive to local environment change within its evanescent field decay length L_p , defined as a distance at which the intensity of electric field decreases in e times. In other words, whether there is a specific biomolecule binding to a receptor in the layer of L_p thickness above the metal film surface can be monitored by the SPP mode change. L_p of the SPP mode was estimated to be ~ 310 nm at $x = 185$ nm where the maximum

electric field E_z located, as shown in Fig. 2(b). The properties of this SPP mode as well as F-P modes, involved in pressure sensing mechanism, will be investigated in detail.

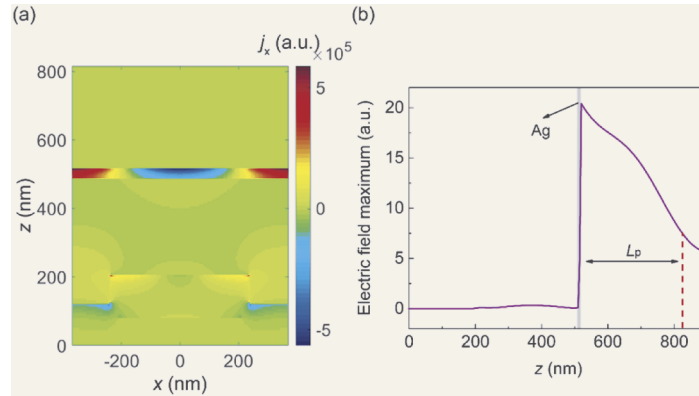


Fig. 2. SPP mode excited on the top surface of the metallic film and used for RI sensing: (a) Surface current density j_x distribution of the mode. (b) Cross-sectional profile of the electric field E_z at $x = 185$ nm.

To explore the potential and optimize the performance of the structure, its reflectance spectrum was calculated sweeping the geometrical parameters P , t , b , and d (Fig. 3). As P increases, all the reflectance dips shift to longer wavelengths, as shown in Fig. 3(a). Particularly, the SPP mode wavelength increases from 552 nm to 954 nm as P varies from 540 nm to 940 nm, while the wavelengths of the first- and the second-order F-P modes increase from 826 nm to 972 nm and from 505 nm to 512 nm, respectively. Expectedly, when the PS spacer thickness t increases, the F-P modes shift to longer wavelengths and the second order F-P mode appears at $t > 200$ nm, while the wavelength of the SPP mode at 756 nm remain unchanged (Fig. 3(b)). At $t = 200$ nm, the SPP mode hybridizes with one of the F-P modes, showing a characteristic anti-crossing pattern. Figure 3(c) clearly shows the effect of the ridge width of grating b on the resonant modes. The spectral position of the SPP mode is immune to the change of b in the simulated range, as the change of the profile keeps the periodicity constant and does not change the value of the momentum supplied by the grating and required for the mode excitation. At the same time, the first-order F-P mode slightly red-shifts as the b increase. When the ridge width of the grating is narrow ($b < 100$ nm), the F-P modes, for which the top surface of the ridge acts as one of the mirrors, are either cease to exist (first-order mode) or diminished in amplitude (second-order mode).

As the metal film thickness d increases, the resonance amplitude of all modes decrease along with a slight spectral blue shift (Fig. 3(d)). The decrease of the magnitude of all the modes can be easily understood as the grating and the cavity involved in their excitation becomes less accessible for the incident wave. Particularly, the dip corresponding to the top-surface first-order SPP mode starts to diminish when d is larger than 25 nm and completely disappears at $d \sim 40$ nm. As the thickness of the metal film becomes greater than its skin depth, the incident field cannot penetrate through it to excite the SPP mode upon diffraction on the grating [24]. An analogous mechanism is involved in the case of the F-P modes.

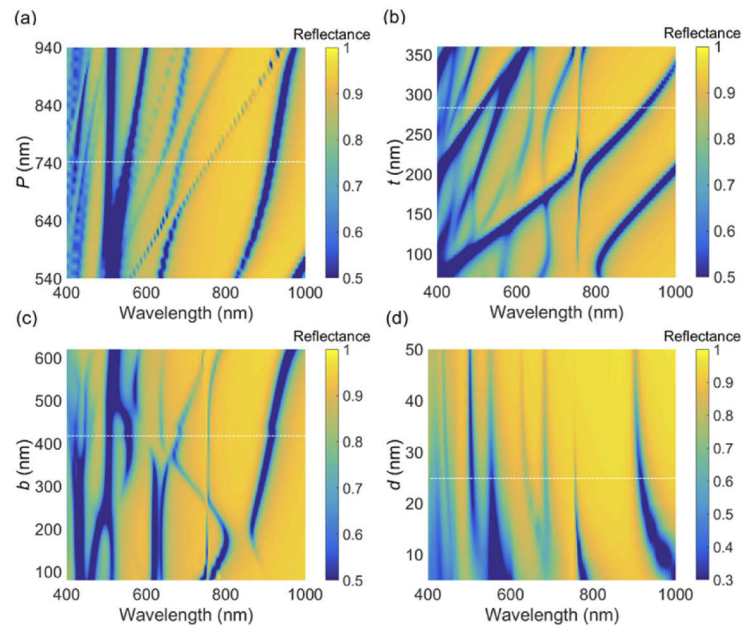


Fig. 3. Dependence of the spectral positions of the modes on the geometrical parameters of the structure: (a) grating period P from 540 nm to 940 nm, (b) spacer layer thickness t from 80 nm to 360 nm, (c) grating ridge width b from 80 nm to 640 nm, (d) silver film thickness d from 5 nm to 50 nm. The white dashed lines in all figures correspond to the spectrum and related parameter set presented in Fig. 1(b).

3. Device fabrication

The fabrication process is presented in detail in Fig. 4. A commercial DVD-R providing a high-quality large-scale grating with a period satisfying the condition for SPP excitation in the visible spectral range was used as an initial template for the fabrication of the sensor heterostructure. The inner grating structure of the DVD disc was exposed by cutting a slit on the side of the disc and then applying a mechanical force to peel the two sides apart. The blue dye covering the grating-shaped polycarbonate profile was washed away with pure ethanol, following which the sample was naturally dried to obtain a clean high-quality line grating with a period of 740 nm and a height of 85 nm (Fig. 4(a)). Importantly, this nanostructure was produced by a low-cost large-scale manufacturing method. A silver film with a thickness of 125 nm was further deposited on the sample, replicating its nanoscale profile and resulting in a well-defined metallic grating, which was observed using SEM microscopy (Fig. 4(b)). Considering the stability of this sensor, gold film is better than silver. Here, an Ag film was selected instead of Au because it is cheaper. Although Ag oxidizes in air, this might not present a problem as the oxidation process is self-terminating at 1–2 nm thickness and furthermore can be avoided by encapsulating it in a few-nm layer of dielectric coating [25].

Then, a large area closely-packed hexagonal PS nanosphere array was self-assembled at the gas/liquid interface using a needle tip flow method [26] and transferred onto the metal grating. After drying the PS sphere monolayer, a clean glass slide was placed on the top of it and the sample was heated to 100 °C to melt the nanoparticles and form a PS spacer layer, which fully fills the space above the grating to produce a smooth flat top surface (Fig. 4(c)). The spacer thickness is dependent on the grating depth and the PS sphere diameter by this method. Here, the height of the PS spacer layer is ~300 nm for 690 nm diameter PS spheres. The last step was

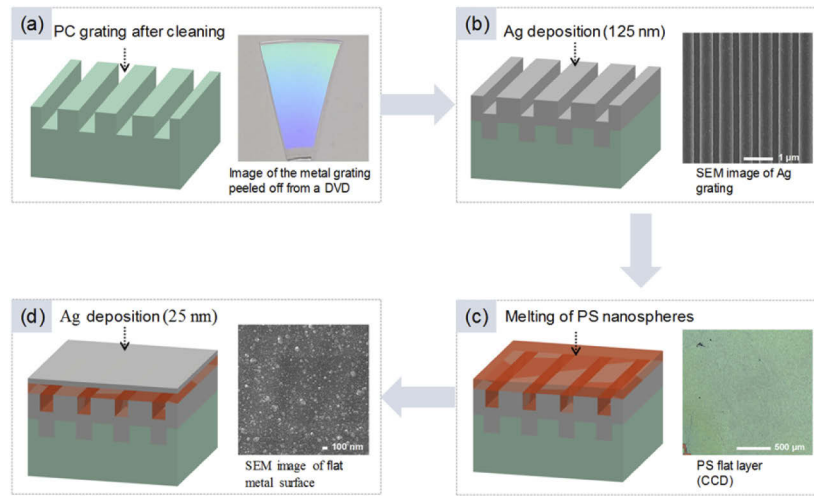


Fig. 4. Fabrication process of the grating-coupled SPR sensor: (a) A PC grating is peeled off from a DVD disc. Inset shows the image of the PC grating. (b) A silver layer with a thickness of 125 nm is sputtered onto the grating. Inset: An SEM image of the Ag-coated PC grating. (c) The grating grooves are filled with polystyrene layer by melting a pre-deposited self-assembled layer of PS nanospheres. Inset: An image of the PS layer taken by an optical microscope with 500x magnification, confirming its uniform structure and a smooth surface. (d) A 25 nm silver layer is deposited on the top of the PS layer. Inset: An SEM image showing the resulting flat Ag surface.

coating the structure with a 25 nm thick Ag film (Fig. 4(d)). An SEM image of the obtained sensing surface confirms the successful fabrication of the device.

To obtain an elastic spacer layer, PDMS is adopted as the spacer using the following method. The ratio of PDMS to curing agent was set to 20:1, to make a softer PDMS film for highly sensitive pressure sensing; then after transferring it onto the metal grating, a clean glass slide was pressed to the surface with the intention to create a smooth surface. After curing in an oven at the temperature of 80 °C for two hours, the glass slide was peeled off. Finally, the surface of the structure was coated with a 25 nm thick Ag film. Since there are no PDMS spheres, the thickness of PDMS is largely dependent on the pressure on the slide when curing it in the oven.

4. Sensing performance

Refractive index sensing was performed to demonstrate the sensing potential of the fabricated grating-coupled SPR platform. The reflectance of the sensor was studied under normal illumination with broadband white light. The spectrum measured in the air environment exhibits the multi-resonant structure predicted in the numerical simulations, but with the SPP dip shifted to a longer wavelength of 824 nm, which is due to a slight geometry difference between the fabricated and idealized simulated structures (Fig. 5(a)). Following the initial idea, this resonance was used to demonstrate the sensing performance of the device. Particularly, the sensing ability of the nanostructure was characterized using a standard benchmark of refractive index sensitivity (RIS) $S = \Delta\lambda/\Delta n$, where $\Delta\lambda$ represents the change in the wavelength position of the resonance with the change of the refractive index Δn . To estimate RIS of the grating-coupled SPR sensor, its reflectance was measured in various liquid environments, particularly in methanol ($n = 1.3290$), 20% ethanol ($n = 1.3450$), 40% ethanol ($n = 1.3550$), 100% ethanol ($n = 1.3611$) and isopropyl ($n = 1.3792$), (Fig. 5(b)). Plotting the spectral position of the SPP resonance as a function of the refractive index of the surrounding and fitting the data with a linear dependence, it was

shown that the sensitivity of 424 nm/RIU was achieved (Fig. 5(c)). This value agrees well with the simulation results confirming the sensing mechanism based on the SPP mode dispersion. Particularly, the numerical simulations show that as the refractive index of the analyte increases, the SPP mode demonstrates a significant red shift of SPP wavelength following Eq. (1), while the spectral positions of all the other modes remain unchanged (Fig. 5(d)).

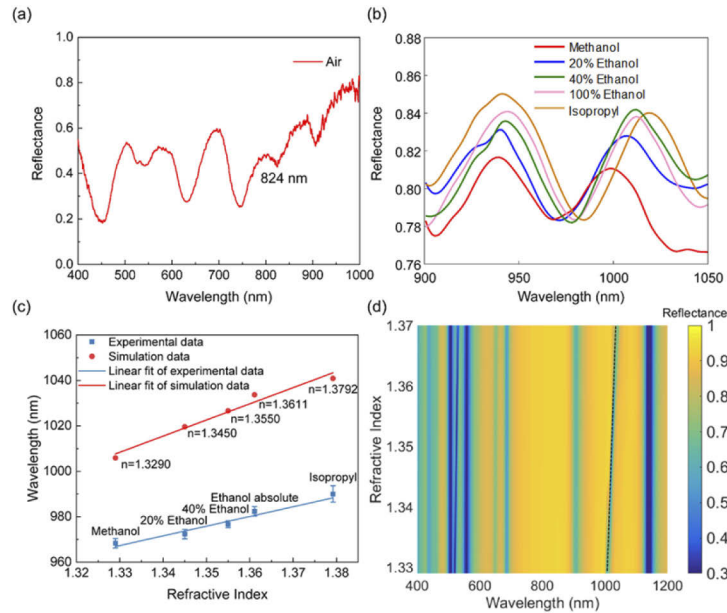


Fig. 5. Refractive index sensing performance of the grating-coupled SPR device. (a) The experimental reflectance spectrum of the sensor measured in air environment. The SPP mode is located at the wavelength of 824 nm. (b) Experimental spectra of the grating-coupled SPR sensor in various environments. (c) The dependence of the spectral position of the SPP mode on the refractive index, where the blue and red dots are the experimental and simulation data, respectively, while the lines present their linear fits. (d) Simulated spectral positions of all the modes as functions of the refractive index of the surrounding, the dashed line marks the spectral shift of the SPP mode.

In order to demonstrate the dual-mode functionality of the grating coupled SPR sensor, an elastic material PDMS was deposited on the metal grating as the spacer-layer instead of PS. As the first step the refractive index sensing functionality was confirmed. The SPP mode located in the air at the wavelength of 756 nm shifts to 930 nm and 941 nm wavelengths when the sensor is interfaced with methanol and ethanol, respectively (Fig. 6(a)). Using a linear fit to the experimental data, the RI sensitivity of this device was calculated to be 494 nm/RIU, the result is shown in Fig. 6(b). Slight shifts of the other dips were observed since the top silver film is too thin and to some extent fragmented, so the properties of the other modes are also affected by the surrounding environment. As the second step, utilizing the elastic properties of the PDMS spacer, pressure sensing functionality of the grating coupled SPR sensor was demonstrated. A quartz slide with a 5 mm × 5 mm opening for optical measurements was placed on the top of the sample, with spiral micrometers at its opposite sides. When an external force was applied on the glass, the PDMS was compressed, which led to the change in the thickness t of the spacer layer and a consequent blue shift in the spectral position of the F-P modes excited between its top and bottom interfaces (Fig. 6(c)). Particularly, under the external force corresponding to the pressure of approximately 0.05 MPa and 0.11 MPa, the F-P mode at the wavelength of 863.15 nm shifted

to 857.52 nm and 848.74 nm, respectively, which corresponds to the wavelength shifts of 5.63 nm and 14.41 nm. Using a linear fit to the experimental data, the pressure sensitivity of the device was calculated to be 131.5 nm/MPa (Fig. 6(d)). At the same time the SPP mode retained its spectral position, which indicates the possibility of simultaneous independent measurement of the refractive index of the analyte and its pressure.

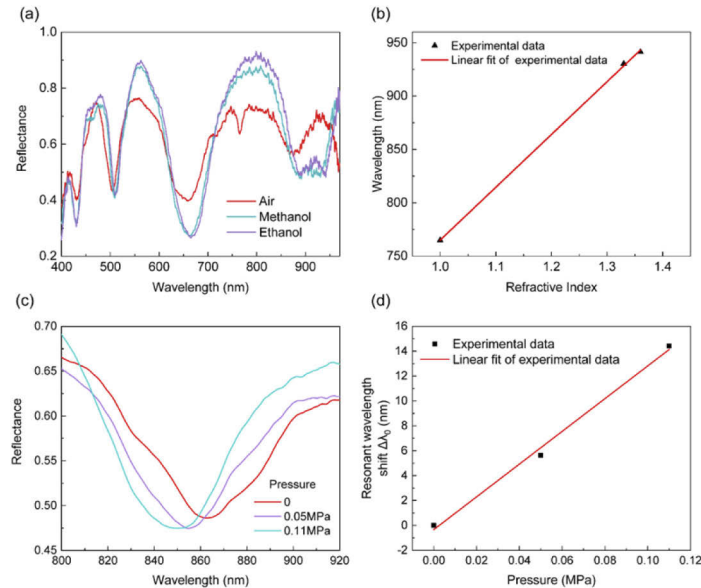


Fig. 6. Experimentally demonstrated dual-mode performance of the PDMS-based grating-coupled SPR device. (a) Reflection spectra of the sensor in various environments. (b) The dependence of the spectral position of the SPP mode on the refractive index of the surrounding, where the black dots are experimental data, and the red line is their linear fit. (c) Modification of the reflectance spectrum under pressure. (d) The relationship between pressure and the resonance wavelength shift $\Delta\lambda_0$.

To further investigate the influence of pressure on the spectral position of the F-P modes, reflectance spectra of the grating-coupled SPR sensor with different spacer layer thicknesses t were simulated. Particularly, it was found that when t decreases, the resonance wavelength of the first-order F-P mode increases linearly with a coefficient of 1.3 (Fig. 7(a), (b)).

Remarkably, when the spacer layer thickness t is set to be small, e.g. less than ~ 40 nm, the F-P modes vanish and a metal/insulator/metal (MIM) surface plasmon mode appears in the gap at the wavelength of 841 nm as a result of coupling of SPP modes at its upper and lower interfaces (Fig. 8(a)). The electric field distribution and current density j_x of the MIM mode are shown in Fig. 8(b) and (c), respectively. As the refractive index change, the MIM mode essentially keeps a constant spectral position at the wavelength of 841 nm, while the SPP mode at a longer wavelength is sensitive to the refractive index variation with a sensitivity of 695 nm/RIU (Fig. 8(d)).

When an external pressure is applied, the thickness of the spacer layer decreases and the MIM resonance shifts to longer wavelengths, oppositely to the blue shift in the case of the F-P modes (Fig. 8(e)). Particularly, a 3 nm decrease of t induces a 37 nm shift of the MIM spectral position. A detailed relationship between the deformation of the elastic layer thickness t and the spectral shift of the MIM resonance is plotted in Fig. 8(f). It can be clearly seen that the MIM mode is more sensitive to spacer layer thickness t variation compared to the F-P modes existing at the larger spacer thickness. Thus, the nanostructure with a thinner elastic layer thickness utilizing

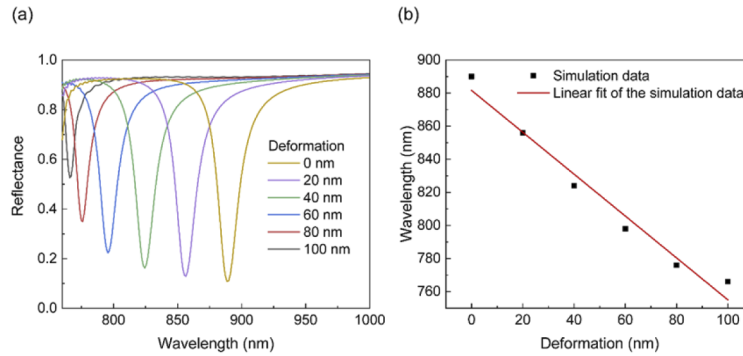


Fig. 7. Simulated performance of the device in the pressure sensing mode. (a) Modification of the reflection spectrum of the sensor with the deformation (decrease) of the spacer thickness t , showing the change of the spectral position of the first-order F-P mode. (b) Spectral position of the first-order F-P mode as a function of the elastic spacer deformation. The black dots are the simulated data points, while the red line is their linear fit.

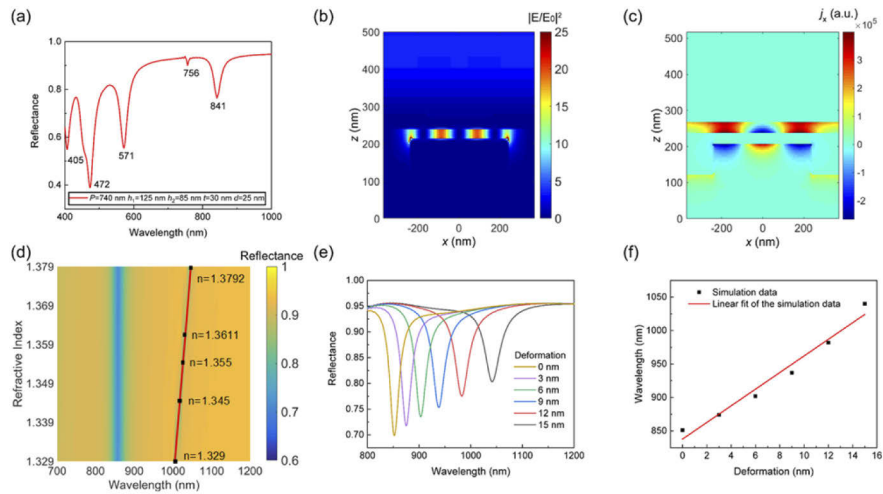


Fig. 8. Pressure sensing performance of the device utilizing MIM SPP mode. (a) Simulated reflection spectra of the device with $P = 740$ nm, $h_1 = 125$ nm, $h_2 = 85$ nm, $t = 30$ nm and $d = 25$ nm, revealing the excitation of the MIM mode. (b) Electric field intensity and (c) surface current density distributions of the MIM mode at $t = 30$ nm. (d) Simulated spectral position of the SPP mode as a function of the refractive index of the surrounding environment, the red line marks the spectral shift of the SPP mode. The black dots are the simulation data. (e) Variation of the reflection spectra with the deformation (thickness decrease) of the elastic layer, showing the shift of the spectral position of the MIM mode. (f) Spectral position of the MIM mode as a function of the elastic layer deformation. The black dots are the simulated data points, while the red line is their linear fit.

SPP and MIM modes can potentially provide better pressure sensitivity, which will be finally determined by the elastic properties of the structure at the nanoscale.

A comparison of the proposed grating-coupled SPR sensor with the reported grating-based counterparts is presented in Table 1. The refractive index sensitivity of the sensors is largely dependent on the periodicity of the grating, the angle of incidence and the operational wavelength range. The sensitivity of our sensor chip shows similar performance to the reported devices

working in the visible range and a somewhat lower sensitivity than those working in the near-infrared. It is the only design, however offering simultaneous and independent sensing of analyte pressure. Furthermore, the pressure sensitivity of our device measured experimentally is estimated to be 131.5 nm/MPa and is better than the pressure sensing performance of single-functionality pressure-specialized sensor from the work of Tathfif et.al. [31]. It should be noted that it is a challenge to precisely prepare an elastic PDMS spacer layer with the thickness less than 40 nm for our sensor operating in the MIM regime, which can potentially provide a better pressure sensitivity. This task along with the search for novel elastic materials and fabrication techniques is a promising direction for a future research.

Table 1. Comparison of Sensor Performance of the Grating-Coupled Plasmonic Sensors

S. No.	Modalities	λ range (nm)	Sensitivity (nm/RIU)	Mode of demonstration	Ref.
1.	Al ₂ O ₃ gratings /Si/Au/Si	600–1400	404.295	Simu.	[27]
2.	Si gratings/SiO ₂ waveguide	1200–1700	497.83	Simu.	[28]
3.	Grating prism	670–770	414.9	Expt.	[29]
4.	Hybrid configuration	1401–1418	1133	Expt.	[19]
5.	Buried grating	954–1054	716	Simu.	[30]
6.	Our configuration	756–941	494	Expt.	

5. Conclusion

In conclusion, we have demonstrated a grating-coupled smooth-surface SPR sensing platform with dual sensing functionality for simultaneous independent sensing of local refractive index and pressure. The device realized on its basis combines high sensitivity characteristics with a number of technological advantages, such as miniature size, easy integration and the possibility of low-cost large-scale production. Smooth surface of the sensor provides a good site for bio-molecular binding and therefore efficient RI-based biosensing of the analyte by optical means via tracking the spectral position of an SPP resonance. Furthermore, the spectral positions of F-P or MIM modes localized in an introduced elastic PDMS layer can be simultaneously monitored for independent optical detection of pressure, affecting the layer thickness. In a prototype device, the refractive index sensitivity of 494 nm/RIU has been demonstrated together with a proof-of-principle pressure sensing functionality. Compared to sensors based on Kretschmann configuration, the proposed structure with flat and smooth surface has a miniature size, is convenient to use, and most importantly provides dual sensing functionality. It is promising for sensing of various biological substances, such as lipid membranes, membrane-bound receptors and lipid rafts.

Funding. National Natural Science Foundation of China (61605082, 61875089); Natural Science Foundation of Jiangsu Province (BE2016756, BK20160969); China Postdoctoral Science Foundation (2017M611654); ERC iCOMM (789340); Engineering and Physical Sciences Research Council (EP/M013812/1); Priority Academic Program Development of Jiangsu Higher Education Institutions.

Acknowledgement. We would like to thank Prof. Xueming Liu, Dr. Tingting Wang and Dr. Yixian Ge for their good advice about this work.

Disclosures. The authors declare no conflicts of interest.

Data availability. Data underlying the results presented in this paper are not publicly available at this time but may be obtained from the authors upon reasonable request.

References

1. H. Reather, *Surface plasmons on smooth and rough surfaces and on gratings*, Springer Tracts in Modern Physics (Springer-Verlag, Berlin-Heidelberg, 1988).

2. A. Olaru, C. Bala, N. Jaffrezic-Renault, and H. Y. Aboul-Enein, "Surface plasmon resonance (SPR) biosensors in pharmaceutical analysis," *Crit. Rev. Anal. Chem.* **45**(2), 97–105 (2015).
3. A. Özkan, N. Atar, and M. L. Yola, "Enhanced surface plasmon resonance (SPR) signals based on immobilization of core-shell nanoparticles incorporated boron nitride nanosheets: Development of molecularly imprinted SPR nanosensor for anticancer drug, etoposide," *Biosens. Bioelectron.* **130**, 293–298 (2019).
4. J. F. Masson, "Surface Plasmon Resonance Clinical Biosensors for Medical Diagnostics," *ACS Sens.* **2**(1), 16–30 (2017).
5. M. Loyez, J. C. Larrieu, S. Chevineau, M. Rimmelink, D. Leduc, B. Bondue, P. Lambert, J. Devière, R. Wattiez, and C. Caucheteur, "In situ cancer diagnosis through online plasmonics," *Biosens. Bioelectron.* **131**, 104–112 (2019).
6. M. Mahmoudpour, J. Ezzati Nazhad Dolatabadi, M. Torbati, A. Pirpour Tazehkand, A. Homayouni-Rad, and M. de la Guardia, "Nanomaterials and new biorecognition molecules based surface plasmon resonance biosensors for mycotoxin detection," *Biosens. Bioelectron.* **143**, 111603 (2019).
7. N. An, K. Li, Y. Zhang, T. Wen, W. Liu, G. Liu, L. Li, and W. Jin, "A multiplex and regenerable surface plasmon resonance (MR-SPR) biosensor for DNA detection of genetically modified organisms," *Talanta* **231**, 122361 (2021).
8. B. Peeters, S. Safdar, D. Daems, P. Goos, D. Spasic, and J. Lammertyn, "Solid-Phase PCR-Amplified DNAzyme Activity for Real-Time FO-SPR Detection of the MCR-2 Gene," *Anal. Chem.* **92**(15), 10783–10791 (2020).
9. Y. F. Chang, W. H. Wang, Y. W. Hong, R. Y. Yuan, K. H. Chen, Y. W. Huang, P. L. Lu, Y. H. Chen, Y. M. A. Chen, L. C. Su, and S. F. Wang, "Simple Strategy for Rapid and Sensitive Detection of Avian Influenza A H7N9 Virus Based on Intensity-Modulated SPR Biosensor and New Generated Antibody," *Anal. Chem.* **90**(3), 1861–1869 (2018).
10. B. Liedberg, C. Nylander, and I. Lunström, "Surface plasmon resonance for gas detection and biosensing," *Sens. Actuators* **4**, 299–304 (1983).
11. E. Kretschmann and H. Raether, "Radiative decay of non-radiative surface plasmons excited by light," *Z. Naturforsch. A* **23**(12), 2135–2136 (1968).
12. P. Arora, E. Talker, N. Mazurski, and U. Levy, "Dispersion engineering with plasmonic nano structures for enhanced surface plasmon resonance sensing," *Sci. Rep.* **8**(1), 9060 (2018).
13. H. Lu, S. Dai, Z. Yue, Y. Fan, H. Cheng, J. Di, D. Mao, E. Li, T. Mei, and J. Zhao, "Sb₂Te₃ topological insulator: Surface plasmon resonance and application in refractive index monitoring," *Nanoscale* **11**(11), 4759–4766 (2019).
14. Y. Vasimalla, H. S. Pradhan, and R. J. Pandya, "SPR performance enhancement for DNA hybridization employing black phosphorus, silver, and silicon," *Appl. Opt.* **59**(24), 7299–7307 (2020).
15. A. S. Lambert, S. N. Valiulis, A. S. Malinick, I. Tanabe, and Q. Cheng, "Plasmonic biosensing with aluminum thin films under the Kretschmann configuration," *Anal. Chem.* **92**(13), 8654–8659 (2020).
16. Y. B. Chen, "Development of mid-infrared surface plasmon resonance-based sensors with highly-doped silicon for biomedical and chemical applications," *Opt. Express* **17**(5), 3130–3140 (2009).
17. X. Xiao, Z. Kuang, J. M. Slocik, S. Tadepalli, M. Brothers, S. Kim, P. A. Mirau, C. Butkus, B. L. Farmer, S. Singamaneni, C. K. Hall, and R. R. Naik, "Advancing Peptide-Based Biorecognition Elements for Biosensors Using in-Silico Evolution," *ACS Sens.* **3**(5), 1024–1031 (2018).
18. S. K. Srivastava, C. Grüner, D. Hirsch, B. Rauschenbach, and I. Abdulhalim, "Enhanced intrinsic fluorescence from carboxidized nano-sculptured thin films of silver and their application for label free dual detection of glycosylated hemoglobin," *Opt. Express* **25**(5), 4761–4772 (2017).
19. S. Joseph, S. Sarkar, and J. Joseph, "Grating-Coupled Surface Plasmon-Polariton Sensing at a Flat Metal-Analyte Interface in a Hybrid-Configuration," *ACS Appl. Mater. Inter.* **12**(41), 46519–46529 (2020).
20. J. R. Sambles, G. W. Bradbery, and F. Yang, "Optical excitation of surface plasmons: an introduction," *Contem. Phys.* **32**(3), 173–183 (1991).
21. S. D. Gedney, Introduction to the Finite-Difference Time-Domain (FDTD) Method for Electromagnetics (Morgan & Claypool, 2011).
22. M. B. H. Othman, M. R. Ramli, L. Y. Tyng, Z. Ahmad, and H. M. Akil, "Dielectric constant and refractive index of poly (siloxane-imide) block copolymer," *Mater. Des.* **32**(6), 3173–3182 (2011).
23. E. D. Palik, *Handbook of optical constants of solids* (Academic press, 1998).
24. S. A. Maier, *Plasmonics: Fundamentals and Applications* (Springer New York, 2007).
25. A. De Rooij, "The oxidation of silver by atomic oxygen," *ESA J* **13**, 363–382 (1989).
26. J. T. Zhang, L. Wang, D. N. Lamont, S. S. Velankar, and S. A. Asher, "Fabrication of large-area two-dimensional colloidal crystals," *Angew. Chem.* **124**(25), 6221–6224 (2012).
27. Y. Li, Y. Liu, Z. Liu, Q. Tang, L. Shi, Q. Chen, G. Du, B. Wu, G. Liu, and L. Li, "Grating-assisted ultra-narrow multispectral plasmonic resonances for sensing application," *Appl. Phys. Express* **12**(7), 072002 (2019).
28. X. Lu, G. G. Zheng, and P. Zhou, "High performance refractive index sensor with stacked two-layer resonant waveguide gratings," *Results. Phys.* **12**, 759–765 (2019).
29. C. Lertvachirapaiboon, A. Baba, K. Shinbo, and K. Kato, "Dual-mode surface plasmon resonance sensor chip using a grating 3D-printed prism," *Anal. Chim. Acta* **1147**, 23–29 (2021).
30. T. Iqbal, H. Tabassum, S. Afsheen, and M. Ijaz, "Novel exposed and buried Au plasmonic grating as efficient sensors," *Wave. Random. Complex.* 1–12 (2020).
31. I. Tathif, A. A. Yaseer, K. S. Rashid, and R. H. Sagor, "Metal-insulator-metal waveguide-based optical pressure sensor embedded with arrays of silver nanorods," *Opt. Express* **29**(20), 32365–32376 (2021).